



CO₂ Hydrogenation to Higher Alcohols over K-Co-Cu-Al: Establishing Structure-Activity Relationships

Vitor D. Lage^{1*}, Carlos A. Ortiz-Bravo², Carla R. Moreira¹, Alexander C. Villegas¹, Rodrigo Bonfim¹, A. Le Valant³, N. Bion³, Fabio S. Toniolo^{1*}

¹ Universidade Federal do Rio de Janeiro, Rio de Janeiro, Brasil. ² Universidade Federal Fluminense, Niterói, Brasil.

³ Université de Poitiers, Poitiers, França. * vlage@peq.coppe.ufrj.br; toniolo@peq.coppe.ufrj.br.

Resumo/Abstract

RESUMO - Este estudo investiga catalisadores K-Co-Cu-Al para a hidrogenação de CO₂ a álcoois superiores, uma rota promissora para a produção sustentável de combustíveis. Demonstramos que composições ternárias otimizadas superam seus equivalentes bimetálicos e a literatura, resultando em um rendimento de álcoois superiores mais elevado de 5,54 mmol·g_{cat}-1·h⁻¹. Este desempenho elevado é atribuído a uma combinação de fatores estruturais e dinâmicos. XANES indica a formação de espinélio de Co-Al, uma fase resistente à redução, enquanto DRX revela partículas de Cu segregadas, resultando conjuntamente em um perfil de redutibilidade aprimorado. As análises pós-reação por XPS e TEM-EDS mostram a migração de Co para a superfície, provavelmente formando partículas de CoCu e indicando uma interação intermetálica intensificada, a qual está associada à adsorção preferencial de CO_x* em sítios de Co. DRIFTS in situ demonstra uma preferência pela rota mediada por formiato sobre o catalisador trimetálico, enquanto a rota mediada por CO é favorecida sobre os catalisadores bimetálicos. *Palavras-chave: álcoois superiores, hidrogenação de CO₂, XANES, DRIFTS*.

ABSTRACT - This study investigates K-Co-Cu-Al catalysts for CO_2 hydrogenation to higher alcohols, a promising route for sustainable fuel production. We reveal that optimized ternary compositions surpass bimetallic counterparts and literature benchmarks, leading to improved HA STY of 5.54 mmol· g_{cat}^{-1} ·h⁻¹. This enhanced performance is attributed to a combination of structural and dynamic factors. XANES reveals Co-Al spinel formation, a reduction-resistant phase, while XRD indicates segregated Cu particles, together resulting in an enhanced reducibility profile. Post-reaction XPS and TEM-EDS show Co migration to the surface, likely forming CoCu particles and indicating enhanced intermetallic interaction, which is associated with preferential CO_x^* adsorption on Co sites. In situ DRIFTS shows a preference for the formate-mediated route over the trimetallic catalyst, whereas the CO-mediated route is favored over the bimetallic catalysts. *Keywords: higher alcohols, CO₂ hydrogenation, XANES, DRIFTS*.

Introduction

 CO_2 hydrogenation has become a realistic process for mitigating CO_2 emissions while converting it into value-added products, such as alcohols and olefins (1). Alcohols with two or more carbons, referred to as higher alcohols (HA), are a versatile (e.g., fuel, solvent, and feedstock), safe, and sustainable option (2).

Previously, we prepared a series of K-Co-Cu-Al catalysts and explored the effect of reaction conditions on their activity and HA yield, reducing undesirable CH₄ selectivity to 22% while increasing HA selectivity to 45%. Co_{1.8}Cu_{0.9}AlO_x, displayed the best catalytic performance (3, 4), ranking among the best reported for HA synthesis (2). Herein, we explore different characterization techniques to establish a robust structure-activity correlation for these catalysts in the CO₂ hydrogenation reaction to HA (CO₂-to-HA).

Experimental

Catalyst Preparation and Evaluation.

Detailed catalyst preparation and evaluation procedures are reported elsewhere (3, 4). The catalysts were prepared

by coprecipitation, thoroughly washed, and calcined at 500 °C. Subsequently, they were impregnated with 1 wt% K and calcined again at 500 °C for 3 h. Samples are denoted as $Cu_{2.6}AlO_x$, $Co_{1.3}Cu_{1.3}AlO_x$, $Co_{1.8}Cu_{0.9}AlO_x$, and $Co_{2.6}AlO_x$ (based on metallic content characterization).

Tests were performed at 30 bar and 250 °C, with varying H_2/CO_2 ratios (3-1.5) and GHSV (10-14 $L\cdot g_{cat}^{-1}\cdot h^{-1}$). Before reaction, catalysts were reduced in H_2 at 400 °C (Cu_{2.6}AlO_x was reduced at 250 °C) for 30 min.

Catalyst Characterization.

Samples were characterized by XRD, ICP-OES, N_2 physisorption, H_2 -TPR, and CO_2 -TPD, detailed elsewhere (3, 4). Morphology and elemental distribution were assessed by TEM (200 kV) and EDS-mapping. Oxidation states and chemical environments were investigated using XPS and XANES (Cu-L_{2,3}, Co-L_{2,3}, and Al-K edges) conducted at the LNLS-IPE beamline. In situ DRIFTS under CO_2 and H_2 flow was employed for mechanistic insights.



Results and Discussion

Catalyst Performance vs. Literature.

Previous work detailed the impact of reaction conditions (3, 4). Briefly (Table 1), Co_{1.8}Cu_{0.9}AlO_x exhibited the best overall performance, favoring HA and inhibiting undesired CH₄, achieving the highest HA space-time yield (STY). Reducing the H₂/CO₂ ratio to 1.5 resulted in peak HA STY of 5.54 mmol·g_{cat}-1·h⁻¹ for Co_{1.8}Cu_{0.9}AlO_x, positioning it as a top-performing Co-based catalyst and among the highest reported HA yields (2).

Table 1. Summary of Catalyst Tests (250 °C and 30 bar) in terms of CO₂ conversion (XCO₂), HA selectivity (S_{HA}), HA STY (STY_{HA}), and CH₄ selectivity (SCH₄).

Catalyst ^a	XCO ₂ (%)	S _{HA} (%)	STY _{HA} (mmol·g _{cat} -1·h-1)	SCH ₄ (%)
Cu _{2.6} AlO _x - A	9	0	0	0 в
Co _{1.3} Cu _{1.3} AlO _x - A	18	18	1.97	54
Co _{1.8} Cu _{0.9} AlO _x - A	17	28	2.90	40
Co _{1.8} Cu _{0.9} AlO _x - B	24	40	4.54	28
Co _{1.8} Cu _{0.9} AlO _x - C	18	45	5.54	22
Co _{2.6} AlO _x - A	10	20	1.23	44

 a A (H₂/CO₂ = 3, 14 L·g_{cat}⁻¹·h⁻¹), B (H₂/CO₂ = 3, 10 L·g_{cat}⁻¹·h⁻¹), C (H₂/CO₂ = 1.5, 14 L·g_{cat}⁻¹·h⁻¹) represent different reaction conditions. / b Cu_{2.6}AlO_x only yielded methanol and CO.

Comparison with recent literature (2, 5) reveals a selectivity vs. conversion trade-off in CO₂-to-HA catalysis Observed (Figure 1). groups include high selectivity/low conversion (Pd/CeO₂, Ru/In₂O₃-ZrO₂, Na-Rh-Fe/ZSM5 and Cu@Na-Beta); high conversion/low selectivity (K-CuZnAl/Zr-CuFe, CuZnAl/K-CuMgZnFe, K-Co-In₂O₃, and CuNaFe); and moderate conversion/ selectivity (Na-Co/SiO₂, Fe-In/K-Al₂O₃, This Work). Regarding HA STY, this work (Co_{1.8}Cu_{0.9}AlO_x) achieves an unmatched 5.54 mmol·g_{cat}-1·h⁻¹, including 3.08 of ethanol. This superior STY is attributed to the catalyst's ability to maintain conversion at higher GHSV. a characteristic shared by other reported catalysts like CuNaFe (28 L·g_{cat}-1·h⁻¹) (6), Cu@Na-Beta (12 L·g_{cat}-1·h⁻¹) (7), and K-CuZnAl/Zr-CuFe (24 L·g_{cat}-1·h-1) (8).Notably, CuNaFe reports ~3.3 mmol·g_{cat}-1·h-1 of ethanol (other HA were irrelevant), a superior ethanol STY, in comparison, yet it was a side product, with the catalyst primarily producing four times more olefins (C2-C8) (6).



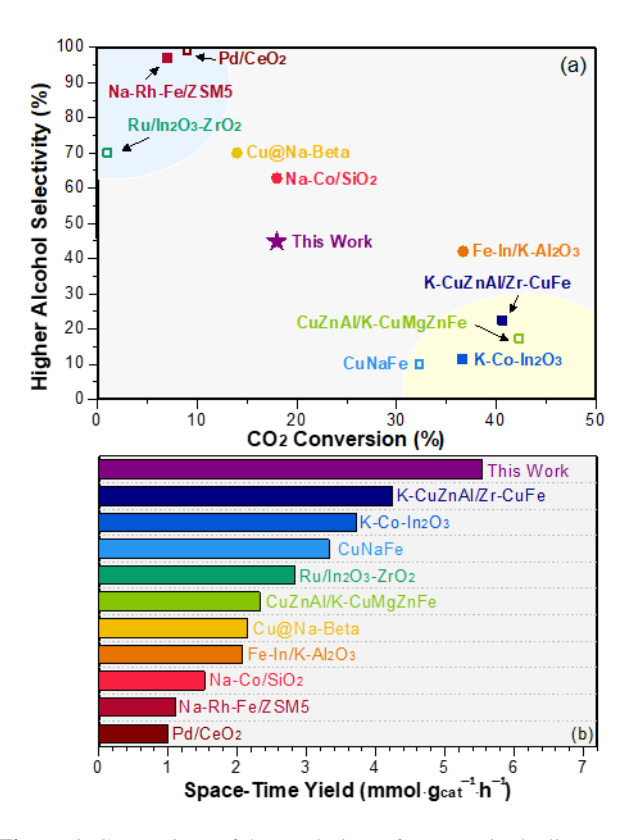


Figure 1. Comparison of the catalytic performance in the literature for the CO₂-to-HA reaction with this work (Co_{1.8}Cu_{0.9}AlO_x).

Understanding K-Co-Cu-Al Structure.

All metallic contents and surface areas (Table 2) were within the expected range for this type of material (9-11). The degree of reduction, calculated based only on Co and Cu contents, indicates that the Co-containing samples were not fully reduced after 1000 °C, suggesting the formation of phases resistant to reduction, such as Co-Al spinel and inverted spinel (10-12). The reduction profile (Figure 2a) of Co_{2.6}AlO_x is indeed shifted towards higher temperatures compared to Co₃O₄ from the literature (13). This effect is somewhat compensated in the trimetallic samples, as Cu can be easily reduced and promote H-spillover onto the catalyst surface, thus favoring reduction (14).

Table 2. ICP, N₂ physisorption, TPR, and CO₂-TPD results.

Catalyst ^a	K content (wt%)	Surface Area (m²·g-¹)	Degree of Reduction (%)	CO ₂ uptake (µmol·g ⁻¹)
Cu _{2.6} AlO _x	0.8	56	99	10
Co _{1.3} Cu _{1.3} AlO _x	0.7	85	89	57
$Co_{1.8}Cu_{0.9}AlO_x$	0.8	69	89	84
Co _{2.6} AlO _x	0.9	78	88	31

^a catalyst's name represents metallic molar ratios.



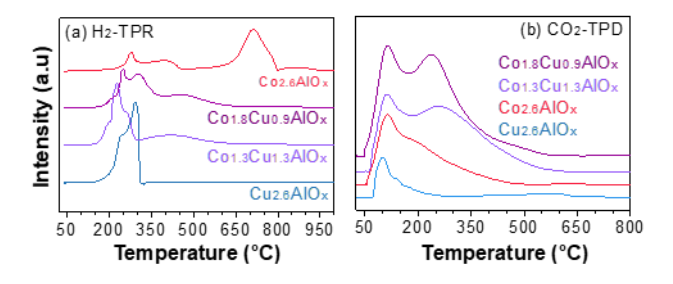


Figure 2. H₂-TPR and CO₂-TPD for the samples.

Interestingly, Co_{1.8}Cu_{0.9}AlO_x displayed the highest CO₂ desorption uptake among the catalysts (Table 2). Most of this contribution in the CO₂-TPD (Figure 2b) is in the temperature range (250-500 °C), attributed to moderate basicity (15), often related to ethanol formation (16). In short, H₂-TPR points to the formation of Co-Al spinel, whereas CO₂-TPD highlights the accentuated basicity of Co_{1.8}Cu_{0.9}AlO_x, which can be associated with its superior activity.

Powder XRD (Figure 3) confirmed the possibility of Co-Al spinel formation on all Co-containing catalysts. For Cu_{2.6}AlO_x, a CuO (tenorite, PDF#48-1548) phase was identified. For Co_{2.6}AlO_x, Co₃O₄ (PDF#43-1003), Co₂AlO₄ (inverse spinel, PDF#38-0814), and CoAl₂O₄ (spinel, PDF#44-0106) are possible matches, as their lattice parameters are nearly identical (11). The trimetallic catalysts presented a mix of CuO and Co₃O₄ (or a Co-Al spinel), with the possibility of Cu-inserting into the Co₃O₄ structure (Co_{3-x}Cu_xO₄, PDF#36-1189), with a slight or no shift in angle due to the small difference in Co and Cu cationic radii (9). The combination of TPR, TPD, and XRD suggests the presence of complex oxide phases; thus, XANES (Figure 4) was employed to investigate the chemical environment.

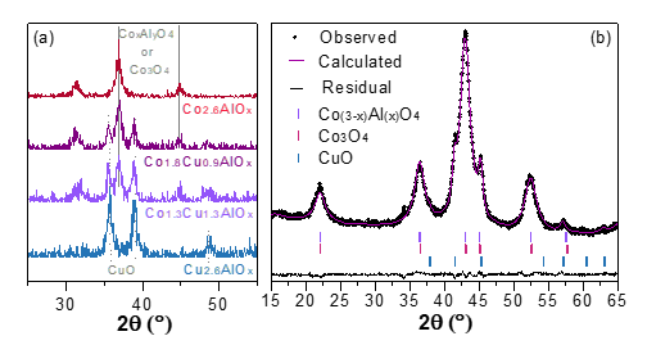


Figure 3. XRD (Cu-K α) for all samples (a), and XRD (Co-K α and fluorescence filter) Rietveld Refinement for Co_{1.8}Cu_{0.9}AlO_x (b).



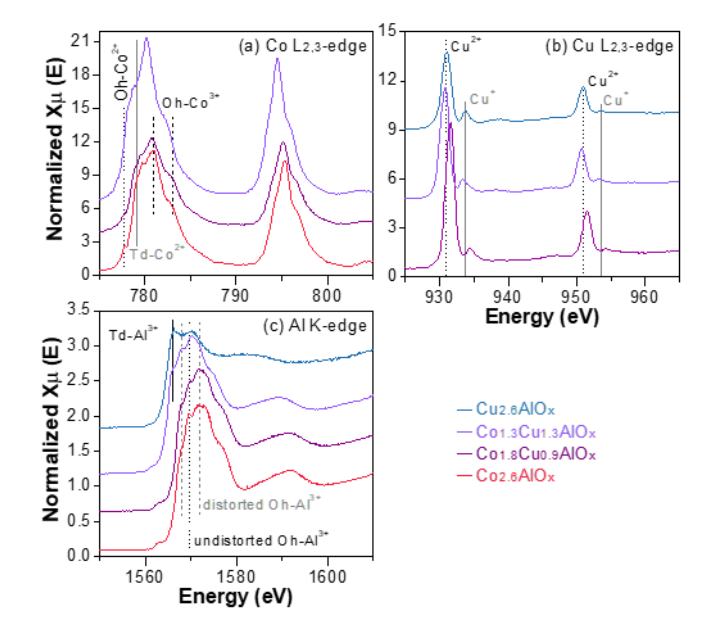


Figure 4. XANES for the samples on the: Al K-edge (a); Co $L_{2,3}$ -edge (b); Cu $L_{2,3}$ -edge (c).

Co L-edge XANES (Figure 4a) shows the presence of both tetrahedral Co^{2+} (Td- Co^{2+}) and octahedral Co^{3+} (Oh- Co^{3+}) cobalt species in the calcined $Co_{2.6}AlO_x$ catalyst, suggesting the coexistence of $CoAl_2O_4$ and Co_3O_4 or Co_2AlO_4 phases (17, 18), consistent with XRD and TPR data. Introducing Cu in $Co_{1.8}Cu_{0.9}AlO_x$ results in a minor presence of Oh- Co^{2+} . Further Cu addition in $Co_{1.3}Cu_{1.3}AlO_x$ led to a greater abundance of Td- Co^{2+} sites, as evidenced by a stronger and redshifted peak at \sim 780.1 eV and a simultaneously weakened and redshifted peak at \sim 782.6 eV.

Cu L-edge XANES (Figure 4b) of Cu_{2.6}AlO_x reveals Cu²⁺ (in CuO) and Cu⁺ species, with no evidence for CuAl₂O₄. In Co_{1.3}Cu_{1.3}AlO_x, Cu²⁺ and Cu⁺ peaks are slightly redshifted, while in Co_{1.8}Cu_{0.9}AlO_x, a blueshift was observed for these peaks. Despite these shifts, the consistent energy separation between the L₃ and L₂ features suggests the stability of both copper oxidation states in the cobalt-containing matrix (19).

Al K-edge XANES (Figure 4c) of Co_{2.6}AlO_x displays features corresponding to both undistorted and distorted Oh-Al³⁺ sites, likely related to CoAl₂O₄, rather than α-Al₂O₃ based on XRD and calcination temperature. Cu addition in Co_{1.8}Cu_{0.9}AlO_x increases the distortion of the Oh-Al³⁺ sites. In Co_{1.3}Cu_{1.3}AlO_x, Td-Al³⁺ sites emerged, and the distorted Oh-Al³⁺ peaks slightly redshifted. In Cu_{2.6}AlO_x, an increased concentration of Td-Al³⁺ sites was observed, consistent with the formation of Al₂O₃ alongside CuO nanoparticles (20). In short, XANES revealed the presence of mixed Co and Cu oxidation states, the formation of Co-Al spinel-like structures, and the influence of Cu addition on the distribution and distortion of these sites. These findings provide a deeper understanding of how Cu incorporation



modifies the Co and Al species within the catalyst framework.

Post-reaction K-Co-Cu-Al.

Comparison between XPS of fresh and post-reaction Co_{1.8}Cu_{0.9}AlO_x underscores significant changes in the catalyst surface (Figure 5). The presented spectra detail the elemental composition of the sample, except for potassium (K), for which no photoemission peak was observed. For surface composition analysis, only Cu and Co were considered due to the overlap of the Al spectral regions with other Co and Cu XPS bands. The calculated surface Co/Cu ratio for the fresh catalyst was approximately 2.7, increasing to approximately 4.9 after the reaction. This increase indicates surface enrichment of Co following the reaction, a finding consistent with TEM-EDS imaging (Figure 6). Recent studies have also reported cobalt surface migration on CoCu catalysts during CO₂-to-HA reaction, attributed to the preferential adsorption of CO_x* onto Co sites (21, 22).

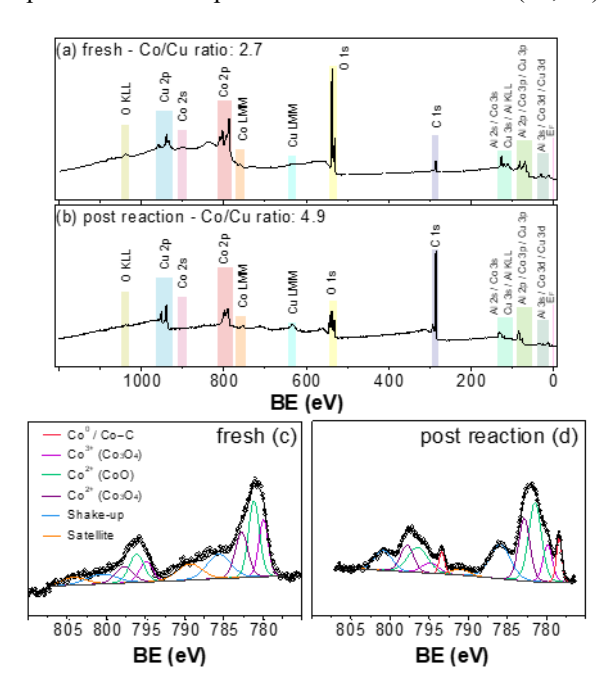


Figure 5. XPS survey of the fresh (a) and post-reaction (b) Co_{1.8}Cu_{0.9}AlO_x, along with their respective Co 2p spectrum (c and d, respectively).

Analysis of the Co 2p spectra reveals a surface enriched in Co²⁺ in the post-reaction catalyst compared to the calcined state. Notably Co⁰ component emerges in the post-reaction spectrum. (14, 16, 21). Concurrently, comparing the Cu 2p spectra for fresh and post-reaction samples suggests partial copper reduction during the reaction (14, 21).

TEM-EDS elemental mapping (Figure 6) of the fresh and post-reaction Co_{1.8}Cu_{0.9}AlO_x samples supports the hypothesis of cobalt migration during the reaction. The fresh



catalyst exhibits regions with segregated Cu, consistent with the CuO phase detected by XRD. Cobalt is uniformly distributed throughout the sample, and the spatial distribution of Al and O correlates with that of Co, reinforcing the Co-Al spinel hypothesis derived from XANES data.

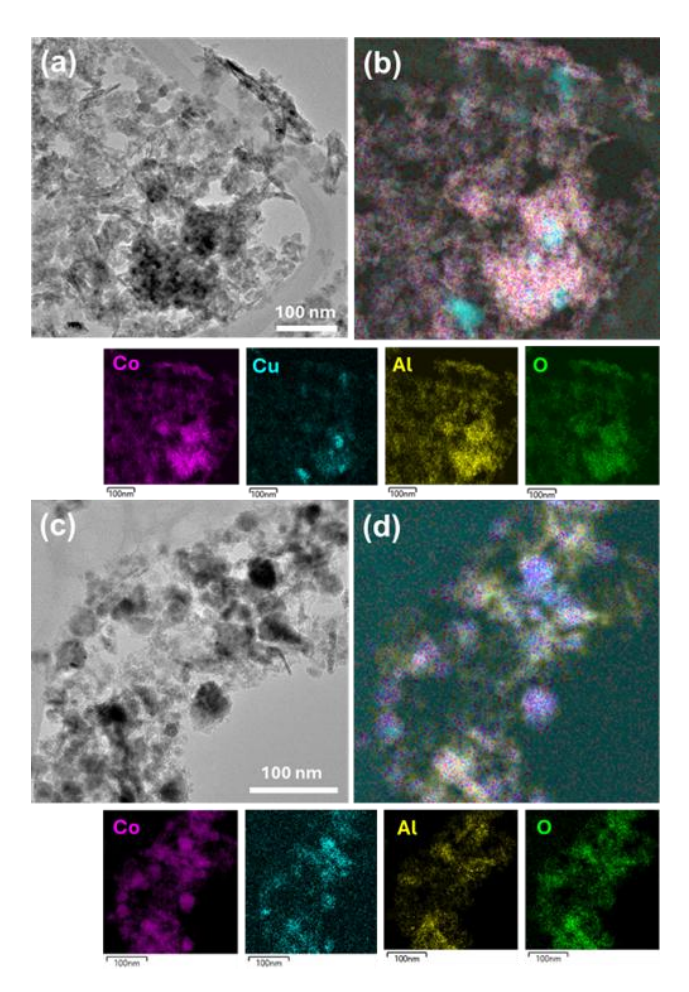


Figure 6. TEM micrographs of the fresh (a) and post-reaction (c) Co_{1.8}Cu_{0.9}AlO_x, along with their respective EDS chemical mappings (b and d, respectively). The colors indicate the elements present in the samples: Cu (blue), Co (pink), Al (yellow), and O (green).

In the post-reaction $\text{Co}_{1.8}\text{Cu}_{0.9}\text{AlO}_x$ catalyst, the dark spots observed in the TEM micrograph (Figure 6c) indicate the presence of both Cu and Co. Cobalt appears less dispersed, forming some spherical agglomerates (Figure 6d). Aluminum forms filamentous structures encircling regions of higher Cu and Co concentration.

Individual elemental distribution maps reveal a markedly different cobalt and copper distribution when comparing the fresh and post-reaction catalysts. Following the CO₂-to-HA reaction, Co_{1.8}Cu_{0.9}AlO_x exhibits a more homogeneous distribution of cobalt and copper, suggesting enhanced Co-



Cu interaction in the post-reaction catalyst. These observations align with XPS findings and literature reports (21, 22). While aluminum is distributed throughout the post-reaction sample, a significant portion exists as isolated aluminum oxide with a filamentous morphology, indicating potential dealumination during the reaction. *Mechanistic Insights*.

In situ DRIFTS near reaction conditions (250 °C, $H_2/CO_2 = 3$) revealed distinct surface intermediates depending on the catalyst composition (Figure 7).

Measurements were taken at ambient pressure, from 1 (bottom) to 150 min (top), after reaction initiation.

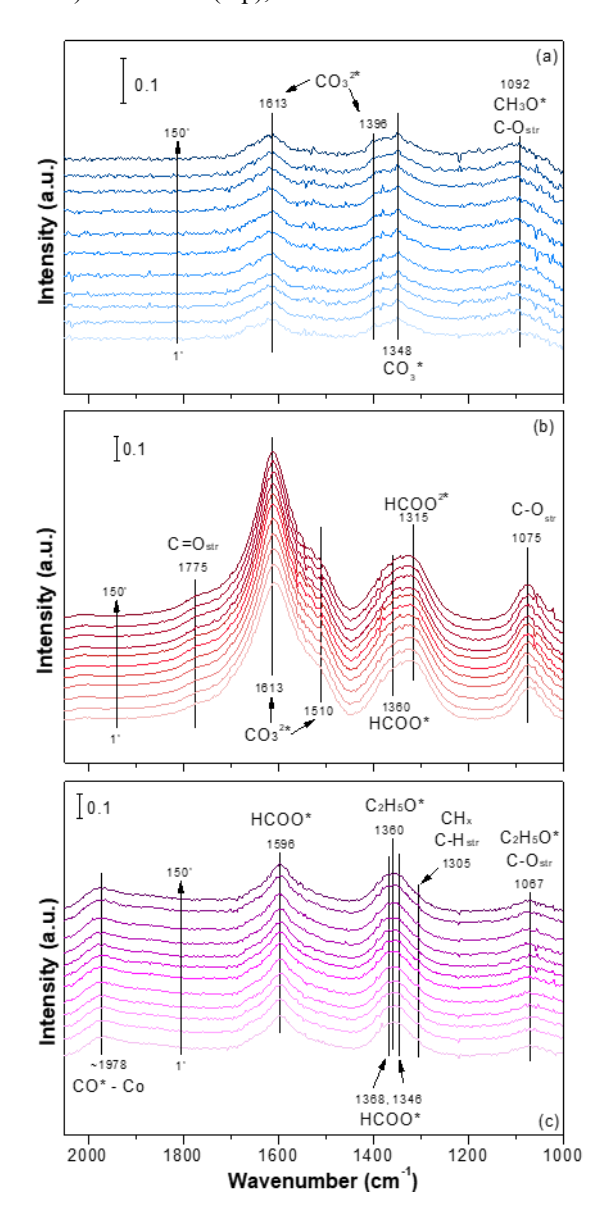


Figure 7. DRIFTS-monitored CO_2 hydrogenation reaction over time (from bottom to top) for $Cu_{2.6}AlO_x$ (a), $Co_{2.6}AlO_x$ (b), and $Co_{1.8}Cu_{0.9}AlO_x$ (c).



Over Co_{1.8}Cu_{0.9}AlO_x, prominent formate species (HCOO*; 1590, 1368, and 1346 cm⁻¹) (23, 24) and likely C₂H_xO* groups (1360 and 1067 cm⁻¹) (24) were observed, alongside CO* adsorbed on cobalt sites (1978 cm⁻¹) (25), suggesting a formate-mediated reaction pathway (26). In contrast, bidentate carbonates (1613, 1510, and 1396 cm⁻¹) (27) were more prevalent over Co_{2.6}AlO_x and Cu_{2.6}AlO_x. Additionally, bidentate formates (1360 and 1315 cm⁻¹) (27) were identified on Co_{2.6}AlO_x. The prevalence of bidentate species on the bimetallic catalysts potentially indicates a dissociative (CO-mediated) adsorption route, which could explain the superior catalytic performance of the trimetallic Co_{1.8}Cu_{0.9}AlO_x catalyst.

Conclusion

In conclusion, we demonstrated that the K-Co-Cu-Al particularly the optimized $Co_{1.8}Cu_{0.9}AlO_x$ composition, exhibits excellent performance in CO2 hydrogenation to higher alcohols. Characterization techniques revealed a complex interplay of factors contributing to this activity. The presence of a Co-Al spinellike structure (XRD, XANES), enhanced cobalt reducibility facilitated by copper (TPR), and optimized basicity (CO₂-TPD) are crucial structural features. Mechanistic insights from DRIFTS suggested a favorable formate-mediated pathway over the trimetallic catalyst. Furthermore, postreaction analysis (XPS, TEM-EDS) indicated dynamic surface restructuring, including cobalt migration and enhanced Co-Cu interaction, highlighting the evolving nature of the active sites under reaction conditions.

Acknowledgements

The authors acknowledge financial support from CAPES (Finance Code 001) and COFECUB (Ph-C 912/18). We thank UFRJ, Université de Poitiers, CNRS, and LABNANO/CBPF for research facilities and assistance. This research used facilities of the Brazilian Synchrotron Light Laboratory (LNLS), part of the Brazilian Center for Research in Energy and Materials (CNPEM), a private non-profit organization under the supervision of the Brazilian Ministry for Science, Technology, and Innovations (MCTI). The IPE beamline staff is acknowledged for the assistance during the experiments 20231628.

References

- 1. R. Ye; J. Ding; T.R. Reina et al., Nature Synth, 2025, 4, 288-302.
- 2. A. Kostyniuk; B. Likozar, Chem. Eng. J. 2025, 503.
- 3. V.D. Lage; A. Le Valant; N. Bion; F.S. Toniolo, *Chem. Eng. Sci.*, **2023**, 281, 158467.
- 4. V.D. Lage; A. Le Valant; N. Bion; F.S. Toniolo in Anais do 22° Congresso Brasileiro de Catálise, Bento Gonçalves, **2023**.





- A.F.J. Tan; M.D. Isnaini; M. Phisalaphong, et al., RSC Sustain., 2024, 2, 3638-3654.
- 6. Z. Si; L. Wang; Y. Han, et al., ACS Sustain. Chem. Eng., 2022, 10, 14972-14979.
- 7. L. Ding; T. Shi; J. Gu, et al., Chem, 2020, 6, 2673-2689.
- 8. Q. Zhang; S. Wang; X. Shi; et al., Appl. Catal. B Environ., 2024, 346, 123748.
- 9. K. Kupková; P. Topka; J. Balabánová, et al., Catalysts, 2023, 13, 107.
- 10. A. Lima da Silva; C.F. Malfatti; I.L. Muller, *ACS Appl. Energy Mat.*, **2023**, 6, 782-794.
- 11. C. Wan; X. Wei; G. Cai, et al., Mol. Catal., 2022, 520.
- 12. N. Aider; F. Touahra; F. Bali, et al., *Int. J. Hydrogen Energy*, **2018**, 43, 8256-8266.
- 13. A. Rabee; C. Gaid; G. Mekhemer, et al., Mat. Chem. Phys., 2022, 289.
- 14. C. Göbel; S. Schmidt; C. Froese, *et al.*, J. Catal., **2020**, 383, 33-41.
- K. An; S. Zhang; H. Wang, et al., Chem. Eng. J., 2022, 433, 134606.
- 16. K. An; S. Zhang; J. Wang, et al., J. Energy Chem., **2021**, 56, 486-495.
- 17. F. Morales, F.M.F. de Groot, P. Glatzel, *et al.*, *J. Phys. Chem. B*, **2004**, 108, 16201-16207.
- 18. B. Serment; C. Brochon; G. Hadziioannou, *et al.*, *RSC Adv.*, **2019**, 9, 34125-34135.
- 19. A.B. Gurevich; B.E. Bent; A.V. Teplyakov, *et al.*, *Surf. Sci.*, **1999**, 442, 0-5.
- 20. J.A. van Bokhoven; H. Sambe. D.E. Ramaker, *et al.*, *J. Phys. Chem. B*, **1999**, 80, 432-440.
- 21. M. Irshad; H. Chun; M.K. Khan, et al., Appl. Catal. B Environ., **2024**, 340.
- 22. S. Liu; C. Yang; S. Zha, et al., Angew. Chem. Int. Ed., 2022, 425, 86-93.
- 23. J.Wang; T. Wang.; Y. Xi, et al., Angew. Chem. Int. Ed., **2023**, 62, 11335.
- 24. Y. Zhou; Y. Wang; H. Liu, et al., ACS Sustain. Chem. Eng., 2024, 12, 3322-3330.
- 25. Z. Wang; C. Yang; X. Li, et al., Nano Res., **2023**, 16, 6128–6133.
- X. Li; J. Ke; P. Li, et al., Chem. Eng. Sci., 2023, 281, 119226.
- S. Bai; Q. Shao; P. Wang, et al., JACS, 2017, 139, 6827-6830.